European Journal of Pharmaceutics and Biopharmaceutics 210 (2025) 114698

Contents lists available at ScienceDirect

European Journal of Pharmaceutics and Biopharmaceutics

journal homepage: www.elsevier.com/locate/ejpb

Research paper

Starch-Based scaffold produced by FDM 3D printing technique as Innovative and biosustainable wound dressing

Franco Dominici [a,1], Anna Imbriano [b,1], Debora Puglia [a], Cinzia Pagano [b,*], Francesca Luzi [c], Aurora Rafanelli [b], Alessandro Di Michele [d], Francesco Bonacci [d], Maria Rachele Ceccarini [b], Sara Primavilla [e], Andrea Valiani [e], Leonardo Tensi [b], Carmen Laura Pérez Gutierrez [b,g], Raquel De Melo Barbosa [f], César Viseras [g], Maurizio Ricci [b], Luana Perioli [b]

[a] Civil and Environmental Engineering Department, University of Perugia, UdR INSTM, 05100 Terni, Italy
[b] Department of Pharmaceutical Sciences, University of Perugia 06123 Perugia, Italy
[c] Department of Science and Engineering of Matter, Environment and Urban Planning, Polytechnic University of Marche, UdR INSTM, 60131 Ancona, Italy
[d] Department of Physics and Geology, University of Perugia 06123 Perugia, Italy
[e] Istituto Zooprofilattico Sperimentale dell'Umbria e delle Marche "Togo Rosati", 06126 Perugia, Italy
[f] Department of Pharmacy and Pharmaceutical Technology, School of Pharmacy, University of Seville 41012 Seville, Spain
[g] Department of Pharmacy and Pharmaceutical Technology, Faculty of Pharmacy, University of Granada 18071 Granada, Spain

ARTICLE INFO

Keywords:
Starch
Thermoplastic filament
Fusion Deposition Modelling (FDM)
Scaffold
Wound healing
Antimicrobial activity

ABSTRACT

Starch is a safe biopolymer, whose use for the production of scaffolds intended for deep wounds treatment is limited, due to its low mechanical and thermal properties. For this reason, until now, it has been used in low amounts and/or in combination with other biopolymers. The aim of the study was to produce thermoplastic filaments (TPS) with high starch content, useful for scaffolds production by Fusion Deposition Modelling 3D printing technique. TPS was obtained by hot melt extrusion from a mixture of starch (70 % w/w) and glycerol (30 % w/w) combined to cationic clay montmorillonite, citric acid and magnesium stearate to improve strength and processability. The prepared scaffold was characterized and compared to other two scaffolds, where the effect of the addition of polycaprolactone (PCL) or methylsulphonylmethane (MSM) (as thermostable model drug) to the blend was evaluated. The mechanical properties were investigated by Brillouin Light Scattering. In vitro studies highlighted that the scaffolds are: i) able to absorb simulated exudates (reaching a hydration of 35 % in 7 days); ii) safe on keratinocytes (viability > 70 %) stimulating their growth; iii) able to inhibit *S. pyogenes* growth.

1. Introduction

Fusion Deposition Modelling (FDM), a hot melt extrusion technique followed by solidification after deposition, is an emerging procedure in the health field for the production of customized oral solid dosage forms [1] as well as implants and prostheses [2]. The exploitation of this technique for the production of scaffolds intended for wound treatment is also of interest [3]. In comparison to traditional wound dressings (e.g. films, foams, gauzes hydrocolloids) [4], scaffolds designed with this technique may offer numerous advantages such as promotion of better and complete healing process as well as the possibility to build a customized formulation according to the patient needs [5,6]. In fact, it is

Abbreviations: BLS, Brillouin Light Scattering; CA, citric acid; CS, Corn starch; DMEM, Dulbecco's Modified Eagle Medium; DMSO, Dimethyl sulfoxide; DSC, Differential Scanning Calorimetry; FBS, Fetal Bovine Serum; FDM, Fusion Deposition Modelling; Gly, Glycerol; HAL, halloysite; HME, hot melt extrusion; MgSt, magnesium stearate; MMT, montmorillonite; MTT, (3-[4,5-dimethylthiazol-2-yl]-2,5 diphenyl tetrazolium bromide) assay; MSM, methyl sulfonyl methane; PBS, phosphate-buffered saline; PCL, poly(caprolactone); PLA, poly(lactic acid); SEM, scanning electron microscope; SWF, simulated wound fluid; TPS, thermoplastic starch.

* Corresponding author.
E-mail address: cinzia.pagano@unipg.it (C. Pagano).
[1] Equally contribution to this work.

https://doi.org/10.1016/j.ejpb.2025.114698
Received 8 January 2025; Received in revised form 5 March 2025; Accepted 16 March 2025
Available online 20 March 2025

possible to design an object of proper shape and dimensions, adaptable to the wound bed and able to reside there for prolonged time in order to promote a more efficient healing process [5]. In particular the possibility of using solvent-free FDM, to prepare scaffolds through a thermoplastic matrix, opens up new perspectives in the development of biocompatible and biosustainable health products.

Taking these requirements into account, the choice of materials is an important aspect to evaluate. The polymeric materials suitable for FDM must be properly processable and mechanically compatible with the tissue [4,7]. Polymers already considered for this application are mainly represented both by synthetic not degradable matrices (e.g. polyethylene and polyurethane) and biodegradable ones as polylactic acid (PLA) and polycaprolactone (PCL) [8]. Considering to develop effective and, at the same time, biosustainable formulations, the use of biopolymers for scaffolds production represents an emerging field of interest [9]. Among biopolymers from natural resources, polysaccharides (e.g. chitosan, hyaluronic acid) attracted considerable interest due to their safety, biocompatibility, biodegradability, abundance in nature and low costs [10]. Also, starch is an interesting polysaccharide that could be successfully employed for the production of filaments for scaffolds production by FDM.

[11,12]. Qiu et al. developed a 3D printing filament based on oxidized maize starch (OMS) using the hot extrusion technique. In vitro biodegradation experiments showed excellent biodegradability, with the material being able to completely degrade within 90 min under the action of amylase [13]. Analogously, in the paper of Zhang et al. found a correlation between rheological properties and printability of oxidized starch with varying carboxyl group contents and molecular chain length [14]. More recently, Hernandez-Tenorio and coworkers reviewed the different possibilities for polysaccharide-based ink formulations [15], including starch, to realize scaffolds for would healing [16], while Gonzalez obtained starch-based pharmaceutical tablets, loaded with a non-soluble drug, by using starches of different botanical origin, drug release properties were found to be dependent of the microstructure, porosity degree, chemical composition (amylopectin/amylose ratio and the presence of other components) of the starch and the ability to the formation of an effective network structure [17]. A more general overview on starch potentialities in additive manufacturing, including its use in food technology, was given by Rong et al. [18].

Literature does not report studies where scaffolds are realized using filaments composed by starch alone or as main component, due to the poor processability and low mechanical properties of this material [19]. Some studies are available dealing with thermoplastic starch combined with polyesters, such as PLA, PCL, or polyhydroxybutyrate, in order to obtain filaments with enhanced processability and mechanical properties. Mahani et al. produced a filament using PLA/TPS blend in the ratio of 40:60 wt./wt. [19]. Ju et al. prepared thermoplastic starch (TPS)/poly (lactic acid) (PLA)/poly (butylene adipate-co-terephthalate) (PBAT) composites for FDM 3D printing technology using a ratio of 50:40:10 wt % (TPS:PLA:PBAT) [20]. Ni et al. developed filaments suitable for FDM based on Astragalus residue powder (ARP)/TPS/PLA in the ratio 11/10/79 wt [21]. Zhao et al. fabricated successfully PCL/starch composites using and amount of starch of 9 phr [22]. Trebuňová et al. produced filaments using a blend of PLA/polyhydroxybutyrate (PHB)/TPS blend in a ratio 75:25:20 wt% [23].

However, these filaments are mainly used for the production of scaffolds for bone regeneration, often loaded with biologically active molecules to obtain functional activity, such as antimicrobial or healing.

The aim of this present work was to develop a thermoplastic starch (TPS) based filament, using high starch content, processable by FDM 3D printing for the production of scaffolds intended for deep wound treatment. High starch amounts (70 % w/w) were combined to additives, such as the cationic clay montmorillonite, citric acid and magnesium stearate useful to obtain a processable filament.

The same composition was also used in combination with PCL or the model drug methylsulphonylmethane (MSM) and their effect on processability of the filament was considered as well. Such filament was then used to produce scaffolds by FDM 3D printing, that were deeply characterized for their hydration behaviour, mechanical properties, cytotoxicity, healing activity, and antimicrobial activity.

2. Materials and Methods

2.1. Materials

Corn starch (Ph. Eur. grade, amylopectin/amylose ratio 74/26) and methyl sulfonyl methane (MSM, purity > 99 %) were purchased from A. C.E.F. (Fiorenzuola d'Arda PC, Italy). Glycerol (Gly), halloysite (HAL), montmorillonite (MMT), magnesium stearate (MgSt) and citric acid (CA, purity > 98.5 %) Calcium chloride ($CaCl_2$, purity ≥ 93.0 %) were purchased from Merck (Milano, Italy). Polycaprolactone (PCL) CAPA 6400 was purchased from Perstorp (Castellanza VA, Italy). Ultrapure water was obtained by reverse osmosis process in a MilliQ system Millipore (Roma, Italy). Other reagents and solvents were of analytical grade and used without further purification. The simulated wound fluid (SWF), pH 6.5, was prepared by dissolving 8.30 g of NaCl and 0.28 g of $CaCl_2$ in 1000 mL of ultrapure water.

2.2. TPS filaments production

TPS filaments were produced by hot melt extrusion (HME) according to a previous work [24,25] using the compositions reported in Table 1.

Methyl sulfonyl methane (MSM) was chosen as model drug. The filaments were prepared as follows: a physical mixture of corn starch (CS) and glycerol (Gly) was prepared by mechanical mixing for 15 min using a dough mixer (450 W). Additives were introduced in the first extrusion step to produce homogeneous granules. This mixture was extruded by using a co-rotating twin-screw extruder Micro Compounder 5 & 15 cc from DSM (Xplore Instruments BV, Sittard, The Netherlands) using the following parameters:

i) temperatures: 134, 140 and 145 °C in the three heating zones,
ii) force: 3,700, 4,000 N,
iii) rotating speed: 30 rpm during feeding, 120 rpm during compounding.

Then, the obtained granules were submitted to a second extrusion, that was performed by using a desktop Pellet Filament Extruder (Extruder Line II + ROBOTDIGG LIMITED) to obtain filaments with a diameter of 1.75 mm (Supplementary Material, Fig. S1) suitable for FDM extrusion. Finally, the prepared filaments were stored at 40 °C for two weeks under a relative humidity (R.H.) of 40 % before use. The same conditions have been considered for the preparation of all the filaments reported in Table 1. The filaments have not been post-treated.

2.3. X-ray powder diffraction (XRPD)

Filaments were firstly dried at 40 °C for 24 hrs and then pulverized with by a knife mill (for 2 min at 40 rpm) prior to XRPD analyses. The study was carried out by using a PANalytical X'Pert diffractometer equipped with an X'Celerator solid-state detector and a sample holder spinning. XRDP patterns were recorded by using random oriented mounts with CuKα radiation, at 45 kV, 40 mA, in the range 3 to 50° (2θ). The estimation of the solid composition in crystalline phases was obtained by X'Pert HighScore Plus (PANanalytical, 2005). The crystallinity was calculated (Eq.1.) as the ratio of area under the crystalline peaks to the entire area of under the diffractogram [26,27].

$$X_c = \frac{A_c}{A_c + A_a} x100 \quad (1)$$

Table 1
Compositions of the filaments produced.

Filament	CS %(wt/wt)	Gly[1] % (wt/wt)	HAL (phr[4])	MMT(phr)	CA[2](phr)	MgSt[3] (phr)	MSM(phr)	PCL(phr)
F0	70	30						
F1	70	30	2					
F2	70	30		2				
F3a	70	30			3			
F3b	70	30			3	2		
F4	70	30		2	3	2		
F4a	70	30		2	3	2		43
F5	70	30		2	3	2	2.5	

Gly[1] = glycerol; CA[2] = citric acid; MgSt[3] = magnesium stearate; phr[4] = parts per hundred of resin (CS + Gly).

2.4. Thermal analysis

DSC analysis of MSM was performed using an automatic thermal analyser (Mettler Toledo DSC821e) and indium standard for temperature calibrations. Holed aluminum pans were employed in the experiments for all samples and an empty pan, prepared in the same way, was used as a reference. The sample (3–6 mg) was weighted directly into aluminum pans and the thermal analysis was carried out in the following heating conditions, in order to simulate the heating–cooling cycles to which the material is submitted during the filament production as well as the extrusion procedure for scaffold production:

i) dynamic heating at 20 °C min^{-1} from 25 to 145 °C, isothermal heating at 145 °C isotherm for 3 min, cooling from 145 to 25 °C at 20 °C min^{-1},
ii) dynamic heating at 20 °C min^{-1} from 25 to 130 °C, isothermal heating at 130 °C isotherm for 3 min, cooling from 130 to 25 °C at 20 °C min^{-1},
iii) dynamic heating at 20 °C min^{-1} from 25 to 210 °C, cooling from 210 to 25 °C at 20 °C min^{-1}.

DSC measurements were also carried out for the produced filaments from 30 to 600 °C at 10 °C/min. Each sample was scanned 3 times.

The thermogravimetric Analysis (TGA) was performed using a Seiko 6300 (Seiko Instruments, Torrance, CA, USA) over a range of temperatures from 30 to 900 °C under nitrogen atmosphere.

2.5. Scaffold production

The most affecting parameters for the FDM 3D printer (Creality 3D Ender-3 V2 Upgraded 3D PRINTER) were investigated by a slicer software (Ultimaker Cura 4.13.1) (Table 2) using a nozzle diameter of 0.4 mm. The final shape of the scaffold is a circular disk with a diameter of 15 mm, thickness 15 mm) with grid infill designed using a CAD model. The prepared filament was extruded by a print head and driven by a motor. The material layer was deposited along an "xy" plane while the extrusion itself advances in the "z" direction.

2.6. Morphological analysis

The morphology of the samples was analyzed by field emission scanning electron microscopy FE SEM LEO 1525 (ZEISS). The samples were deposited on aluminum support using conductive carbon adhesive tape. Before the analysis, the samples were metalized with a thin layer of chromium (8 nm). Measurements were carried out using a standard Everhardt-Thornley secondary electrons detector at 5 kV.

Table 2
Setting parameters for scaffold printing by 3D FDM.

Settings	Value
Nozzle temperature (extrusion temperature)	205 to 220 °C
Flow material	85 to 88 %
Infill density	40 to 50 %
Print speed	12 to 30 mm/s
Fan speed	30 to 50 %
Plate temperature	55 to 65 °C

2.7. Brillouin microscopy

Brillouin spectra have been acquired using the high-contrast version of the tandem Fabry-Perot interferometer (TFP2 HC, JRS Scientific Instruments, Tablestable Ltd, Mettmenstetten, Switzerland). In brief, a diode-pumped solid-state laser by Spectra-Physics Excelsior, operating at a wavelength of 532 nm, is first passed through a temperature-controlled etalon (TSED TCF-1, JRS Scientific Instruments, Tablestable Ltd., Mettmenstetten, Switzerland) to reduce secondary laser modes. The beam is then focused on the sample using a customized CM-1 confocal microscope from JRS Scientific Instruments, equipped with a coaxial LED for illuminating and observing the sample surface. A 20x objective (Mitutoyo, numerical aperture NA = 0.42) is used to focus and collect the backscattered light, which is sent to the high-contrast version of the tandem Fabry-Perot interferometer. The spectral resolution of the interferometer is about 100 MHz, while the spectra were measured across 512 channels, yielding a sampling step of around 90 MHz, given the used free spectral range (FSR) of approximately 24 GHz. This FSR value was chosen to resolve the whole Brillouin peak, typically located at around 18.5 GHz, by adjusting the mirror spacing to a distance of 6 mm. More details of the instrumental setup can be found in [28].

2.8. Swelling studies and matrix erosion

Filaments and scaffolds hydration capacity, as well as the erosion ability, were evaluated *in vitro*. One cm of each filament (or scaffold) was weighed (W1), immersed in 1 mL of SWF and maintained at 37.0 ± 0.1 °C for fixed times (T1: one week; T2: one month; T3: two months; T4: three months; T6: nine months and T7: eighteen months) were established. At each check point the sample was dried using filter paper to remove the excess of SWF and weighed (W2). The hydration percentage was calculated according to Equation (2) (Eq. (2):

$$Hydration\% = (W2 - W1)/W2x100 \quad (2)$$

Then the sample was dried at 37 °C for 48 h in oven and then kept in desiccator under $CaCl_2$ for 48 h, then reweighed (W3). The matrix erosion (DS%) was calculated according to Equation (3) (Eq. (3), respectively:

$$DS\% = (W1 - W3)/W1x100 \quad (3)$$

2.9. In vitro effect on cells

HaCaT cell line (human immortalized keratinocyte, purchased from I.Z.S.L.E.R. Istituto Zooprofilattico Sperimentale della Lombardia e dell' Emilia Romagna) was used for the *in vitro* cell experiments. For Thiazolyl blue tetrazolium bromide (MTT assay), HaCaT cells were seeded onto a

96-well plate at a density of 1×10^4 cells/well with Dulbecco's Modified Eagle Medium (DMEM) complete medium containing 10 % Fetal Bovine Serum (FBS). The stock solution of each sample was prepared using an amount of filament or scaffold immersed in DMEM with a ratio of 10 mg of sample per 1 mL DMEM.

Filaments and scaffolds samples were incubated at 40 °C for 24 h then centrifuged 4000 rpm for 30 min and the supernatant with four different dilutions was incubated with cells for 24 h. Then, MTT reagent was dissolved in Phosphate-Buffered Saline (PBS) 1X and added to the culture at 0.5 mg/mL final concentration. After 3 h of incubation at 37 °C, the supernatant was carefully removed and formazan salt crystals were dissolved in 200 μL dimethylsulfoxide (DMSO). After 30 at 37 °C min the absorbance expressed as optical density (OD) was measured spectrophotometrically at 540 nm using an automatic microplate reader (Eliza MAT 2000, DRG Instruments, GmbH). Each experiment was performed two times in triplicate. Cell viability was expressed as a percentage relative to that of the control cells, as described in literature [29]. A one-way ANOVA test was performed using the Graphpad program (GraphPad Prism 9.2.0.332, GraphPad software, San Diego, CA, USA).

The effect on wound closure was investigated by CytoSelect™ Wound Healing Assay Kit (Cell Biolabs, Inc., San Diego, USA). HaCaT cells ($3x10^5$) in DMEM were seeded into 24-wells tissue culture plate. A properly treated inserts were put in each well with their "wound field" aligned in the same direction. The plate was incubated for 24 h to allow the cells adhere and reach the confluence [29]. After removing the inserts from the wells, the medium was removed, the wells washed twice with PBS 1X to remove dead cells and debris. Finally, the cells were treated with different concentrations of the samples for further 6, 12 and 24 h. Migration into the wound field was measured by using manual fixing with cell stain solution. To analyze cell migration, a picture for each scratch was taken at the same area of cells at 6, 12 and 24 h of the incubation time. Representative images focused on the center of the wound field were photographed. Three sets of experiments were performed. The influence of compounds on wound closure was compared to untreated control (only complete medium).

MSM and CA quantification in the samples obtained by scaffold incubation overnight in DMEM was performed by NMR. NMR spectra were recorded on a Bruker Avance NEO 400 spectrometer equipped with a PI-HR probe (400 MHz for 1H) with a z gradient coil. In the case of the quantitative NMR analysis, the samples were suspended in SWF (10 mg/mL) for 24 h at R.T. Subsequently, 540 μL of the suspension of the samples and 60 μL of a solution 60.35 mM of maleic acid in D_2O were transferred inside the NMR tubes for a total volume of 600 μL. The quantitation of the analytes was carried out using the solvent suppression pulse sequence "noesygppr1d" from the Bruker library. The monodimensional ^1H NMR pulse sequence is a normal ^1H NMR with a low-energy soft pulse on the solvent resonance (50 Hz pulse window) prior to the excitation pulse. The soft pulse is necessary to suppress the solvent signal (90 % H_2O/ 10 % D_2O) that could distort the spectrum baseline preventing the correct integration of the analytes' peaks. The MSM and CA concentrations were obtained by relative integration of the resonances of the analytes versus the signal of the internal standard.

Maleic acid was used as internal standard as: i) it is a common and broadly accepted NMR standard in aqueous samples; ii) it is extremely soluble in water and thermally stable; iii) from the spectroscopic point of view, in D_2O, it is characterized by a sharp single peak resonating at 6.1 ppm which is far enough from the solvent signal and it is in a region where, in our samples, there is no overlapping with other peaks (Supplementary Material, Fig. S2).

All the spectra were acquired using 32 k points, 8 scans and were processed with 32 k points and a line broadening of 0.3 Hz. The experiments were carried out with a total recycle delay of about 45 s. In the case of the filament F5, three replicates were carried out.

2.10. Antimicrobial activity

The antibacterial activity was evaluated against 15 strains, including Gram + bacteria, Gram − bacteria and yeasts, using agar well diffusion technique [30]. All the tested strains were bought from Microbiologics, St. Cloud, MN, USA. *Propionibacterium acnes* was bought from Mecconti S.A.R.L. Sp. z o.o., (Warsaw, Poland). For each organism, 100 μL of a 0.5 McFarland in 0.9 % sterile saline solution suspension were distributed on Mueller-Hinton agar (MHA)/Mueller-Hinton agar 5 % defibrinated sheep blood (MHAB) plates (Oxoid Limited, Basingstoke, UK) by a swab. The filaments and the scaffolds were put on the plates that were incubated according to the growth conditions shown in Table S1 in the Supplementary Material. After the incubation, the diameters of the inhibition halo were evaluated by a gauge (mm).

3. Results and discussion

3.1. TPS filaments production and characterization

Starch is a versatile biopolymer that can be considered for the production of thermoplastic filaments. However, the main limitation for this purpose may be represented by the lack of a semicrystalline structure which may be responsible for softening of the matrix with difficult solidification during subsequent cooling. Furthermore, starch is also sensitive to other external factors, such as humidity, which could affect both the viscosity and ageing of the plasticized material. This could have a negative effect on the processability of the material. On the basis of these constraints, compositions and processing conditions for thermoplastic starch-based filaments production were therefore optimized as follows (Scheme 1). Initially, starch was combined to glycerol (Gly) using a starch/Gly ratio of 70/30 wt/wt % and thermally processed in the extruder. However, the obtained thermoplastic starch filament (TPS) did not possess suitable processability for thermal extrusion through the printer nozzle. Thus, some further components were considered in order to modify the thermomechanical properties of the material and adapt it to FDM 3D printing. For this objective, two inorganic cationic clays were considered: the lamellar clay montmorillonite (MMT) and the tubular clay halloysite (HAL), largely used as fillers in polymeric mixtures for their ability to improve the mechanical strength and durability, as well as the thermal stability [31–33].

Citric acid (CA) was also selected as further additive. Literature data document that CA addition to corn starch filament, plasticized with Gly, allows to obtain a product with enhanced thermal stability, useful for the extrusion process. Moreover, it has been observed that CA is able to establish strong hydrogen-bond interaction with corn starch preventing the re-crystallization (i.e. retrogradation) [34]. Magnesium stearate (MgSt) was then used as additional lubricant in the final mixture to promote the easy flow and release of material from the nozzle.

The produced filaments (compositions reported in Table 1) were deeply studied in order to evaluate their suitability for FDM 3D printing. Considering that during FDM extrusion the processed materials are treated with rather high temperatures, the drug (generally mixed to the polymer before HME treatment) must be thermostable in order to avoid the degradation during processing. Thus methylsulfonylmethane (MSM), an organosulfur compound known for the anti-inflammatory and antioxidant properties, was selected as model drug [35]. MSM thermal stability was evaluated by differential scanning calorimetry analysis. The thermal profile of MSM submitted to heating–cooling cycles (see par. 2.3.) to simulate the thermal extrusion was registered. In the thermogram reported in Supplementary Material Fig. S3, it is possible to observe that MSM does not undergo to substantial modification, except for a limited crystallinity decrease, that does not affect the activity. Considering the effect on clay addition on the final filament characteristics, it was observed that HAL addition to starch is responsible for an increase of the filament stiffness (filament F1) and this is also confirmed by literature data [36].

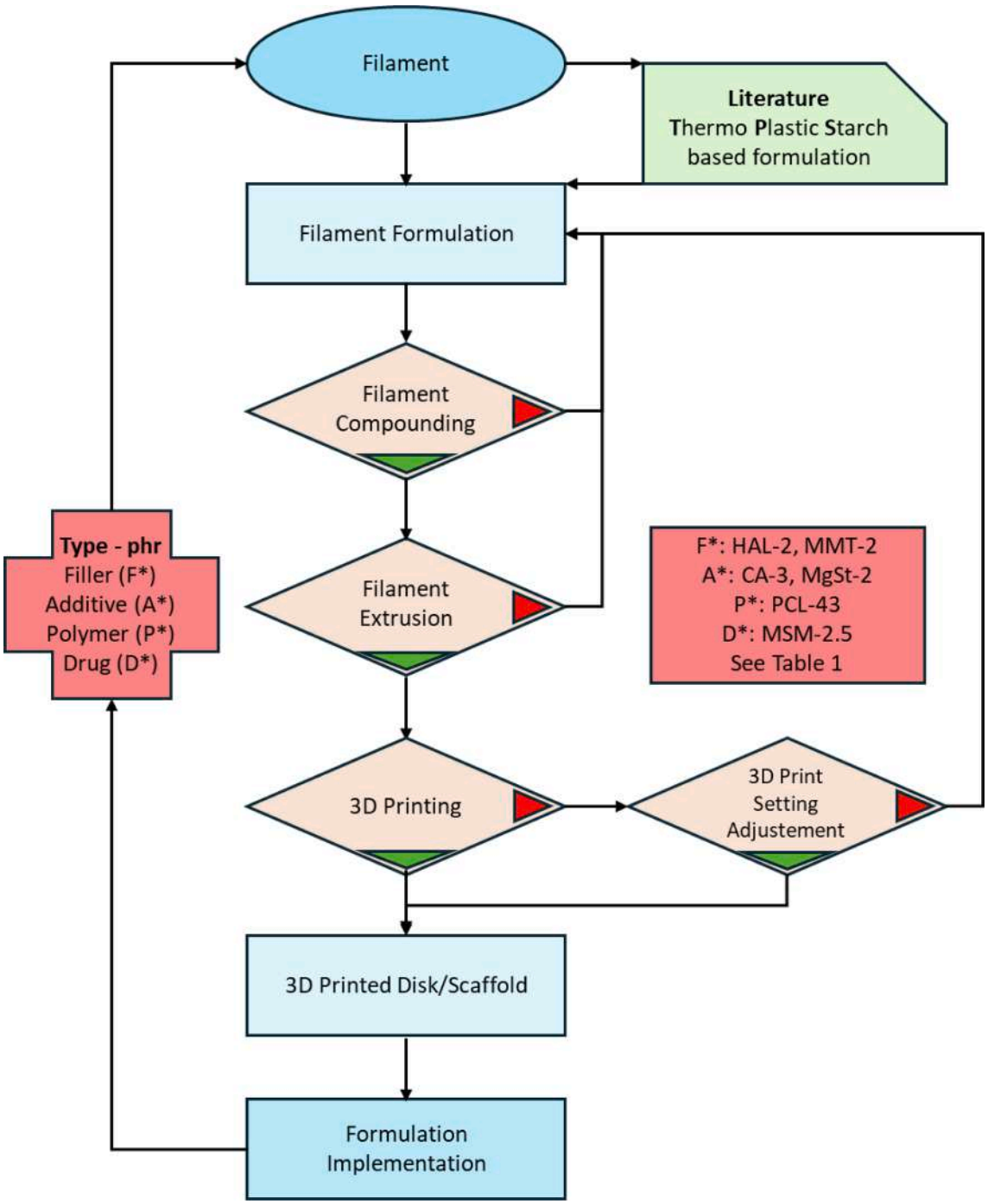

Scheme 1. Flowchart of the research method followed.

The produced filaments were then submitted to deep characterization in order to find the most suitable to be used for scaffold production. In agreement to Ghanbari et al. [37] the main diffraction peaks visible in all the XRDP patterns can be ascribed to the plasticizing process of CS with Gly (Fig. S4, Supplementary material). The main reflection in each diffractogram at $2\theta = 23.0°$, $17.3°$, $20.0°$, $18.3°$ and $20.4°$ for F0, F1, F2, F4 and F5, respectively, suggested that the crystalline structure of each filament follows V_H-type pattern [37]. The presence of MMT in F2, F4 and F5 is confirmed by weak diffractions at $2\theta = 7.0$ °and 27.4°. HAL possess a reflection around $2\theta = 13.0°$, which in this case coincides with a reflection ascribable to other ingredients (probably CS or Gly), being therefore, masked. No other mineral diffractions are detectable, probably due to the low amount of MMT and HAL in the total filament composition. MSM is not detectable due to its amorphous form, since during the preparation process this active is melted. Regarding crystallinity (Fig. S4, Supplementary material), samples F1 and F5 showed smaller crystallinity values in comparison to F0. F3b showed the lowest crystallinity as a result of the incorporation of MgSt. This effect was attenuated in samples F4 and F5, due to the presence of crystalline phases (MMT). Some studies show that TPS without clays does not have any impact on CS crystallinity and retrogradation. However, this result suggests that when CS is plasticized with Gly, clays have the possibility of interacting with polymeric chains of starch, obstructing their rearrangement to a certain extent, and consequently preventing retrogradation of the polymeric matrix. This could be attributed to the fact that the filament has absorbed humidity from the environment, according to

Camila et al. [38]. In addition, the results suggest that the addition of the different additives (CA, MgSt, MSM) also decrease the crystallinity of the samples [39]. Particularly, CA has proven to increase the thermal profile and plasticization of TPS, ultimately slowing down the crystallization [34,40]. It should be underlined that the addition of plasticizing additives aimed to reduce the mechanical strength of the filament and favours its extrusion. In this sense, both Gly and MgSt fulfil this function (Fig. S4, Supplementary material). The crystalline values in the presence of clays (F1, F2, F4, F5) are slightly higher than F3a and F3b, due to the presence of particular crystalline minerals that do not melt during processing. Then, the thermal properties of the filaments were evaluated by both DSC and TGA analyses. DSC was considered as a valuable method to identify transition temperatures (Fig. S5, Supplementary Material). In the case of F0, wide endothermic events probably due to the combination of physisorbed water evaporation and CS and Gly melting were observed. CA shows an endothermic event at ~ 160 °C [41], which can be modified when combined with CS and other additives (thus explaining the results of F4 and F5). The endothermic event starting around 140 °C in F3b can be ascribed to the presence of MgSt, whose melting range has been reported to be around 120–150 °C [42]. This event can also be detectable in F4 and F5. No exothermic events are detectable in this temperature range, pointing out that no degradation events occur for any ingredient. The first scan evidences the presence of an endothermic peak, due to the residual plasticization of the TPS based materials, that was almost complete in the case of F5 sample, loaded with the model drug MSM. The presence of melting peaks at lower temperatures (between 60 and 90 °C) are ascribable to MgSt (recrystallized during the cooling step), that partially covered the signal related to TPS glass transition (T_g). The TGA curves (Fig. S6A, Supplementary Material) of TPS filaments reported in Table 1 show three main steps in the ranges 60–250 °C, 250–350 °C and 350–600 °C. The first ramp accounted in all cases for approximately 20 % of weight loss, corresponds to the water desorption, in agreement with the DSC results (Fig. S5, Supplementary Material). The second step, the main weight loss (65 % of total mass), occurring from 250 to 350 °C, can be ascribed to the dehydration of polysaccharide hydroxyl groups followed by the polymer decomposition, as reported in literature [43]. The delimitation of this stage was obtained in the derivative curve DTG (Fig. S6B, Supplementary Material) that shows a well-defined peak, which suggests that this degradation happened as a single mechanism of decomposition. Finally, a slow weight loss occurs starting from 350 °C until reaching stability at temperatures higher than 600 °C. At these temperatures, the degradation products of the previous event continue to degrade. The residual mass is represented by the inorganic components of TPS filaments, namely MMT and HAL [44]. In the first step, F0 filament shows higher weight losses in comparison to the other filaments, due to the absence of additives. F1 profile is similar to F0 in the whole range, indicating that HAL does not improve the thermal resistance of the filament. On the contrary, the presence of MMT (F2) seems to improve the thermal resistance, especially during the first weight loss step, starting the second degradation step at slightly higher temperatures. This makes sense when looking at the TGA profiles of these clay minerals on their own, MMT having less weight loss than HAL [45,46]. The increased thermal stability of the filaments containing MMT could be attributed to interactions between MMT and CS, responsible for a more compact internal structure [47]. A higher mass loss was reported for the filament F3a during the second step, suggesting that its composition is more thermally labile [48]. Nevertheless, this lability can be compensated by the addition of MMT, since the F4 and F5 filaments weight loss profile was similar to those without CA and even showed higher residual mass.

In vitro assays were then performed in order to evaluate the water absorption capacity of the filaments (expressed as hydration %), as well as their ability to undergo erosion (DS%) once in contact with a fluid simulating the wound exudate. The results of the hydration studies (Fig. 1A) show that all filaments were capable to absorb fluids and this is attributable to the hydrophilicity of starch, able to bind the water molecules due to high amount of hydroxyl groups. However, some differences can be detected and, considering that all the filaments are constituted by starch and Gly in the same ratio, these are attributable to the presence of the other additives in their compositions (Table 1). F0 (without CA) and F3a (containing CA) show the same profile and the lowest value for hydration ability (~45 % maintained for all the experiment). Considering the results coming from DS % assay, F0 shows a limited erosion degree (about 25 % during all the experiment), suggesting filament integrity and compactness (Fig. 1B). F3a shows a high % of erosion (~50 %) probably due to CA presence in the composition (Fig. 1B) as, due to its hydrophilicity, it could be hypothesized that CA is

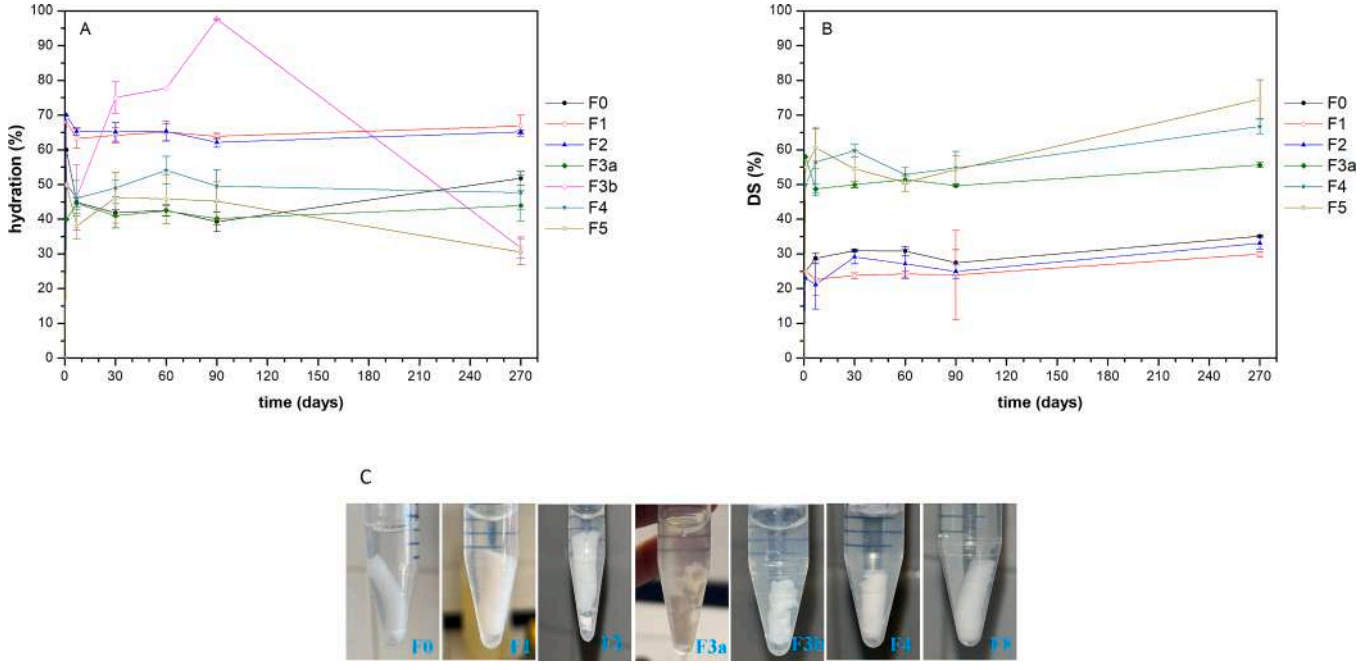

Fig. 1. Results of **A**) hydration (%) and **B**) DS, Degree of swelling (%); **C**) Pictures of the filaments during swelling experiments.

responsible for the water penetration in the inner spaces with consequent enhanced erosion compared to F0.

F1 and F2 show a hydration value of ~ 65 %, maintained constant during all the experiment, attributable to the presence of HAL and MMT clays for F1 and F2, respectively. As the swelling property of these two clays is well described in literature [49], it can be assumed that their presence in the filament might be responsible for a better filament swelling, compared to TPS filament without clays (F0). Considering DS % results (Fig. 1B), the two filaments F1 and F2 undergo limited erosion (< 30 %), attributable to the clays presence, responsible of filaments compactness and integrity. F3b shows the highest hydration percentage reaching ~ 95 % at 90th day (Fig. 1A). However, the profile is not regular and this is attributable to the filament loss of integrity during the incubation in SWF (Fig. 1C) probably this is due to the coexistence of hydrophilic/soluble CA and lipophilic MgSt responsible for filament fragmentation, for this reason it was not possible to report the DS% profile. This filament was then excluded from the study. F4 and F5 show a hydration percentage, respectively, of ~ 50 % and ~ 45 %, maintained during all the experiment. Compared to F1 and F2, the hydration is reduced, due to the presence of the lipophilic MgSt responsible for the decreased water uptake (Fig. 1A). Considering the results deriving from matrix erosion assay (Fig. 1B) the profiles are similar to F3a and could be attributed to CA presence able to promote the water penetration and consequent erosion.

In order to select the most suitable filament for scaffold production, extrusion attempts by FDM were carried out. Extrusion trials demonstrated that, despite F1, F2 and F3a are able to absorb high SWF percentages maintaining the integrity, however they resulted not suitable for extrusion. In fact, problems of nozzle obstruction occurred during their processing by FDM mainly due to starch thermal susceptibility during the extrusion. In the case of F4 and F5, better results were obtained, as the presence of both CA and MgSt allowed to obtain a more processable filament and for this reason used for the next studies. Together to them it was interesting to develop a further filament by introducing a compatible biodegradable polymer in F4 composition. Thus, poly (ε-caprolactone, PCL) was selected and the filament named F4a was produced (Table 1). PCL is a polyester largely employed in many health products, especially implantable systems, due to its controlled biodegradability, as well as safety [50–53] thus it was considered interesting to evaluate its influence in the filament

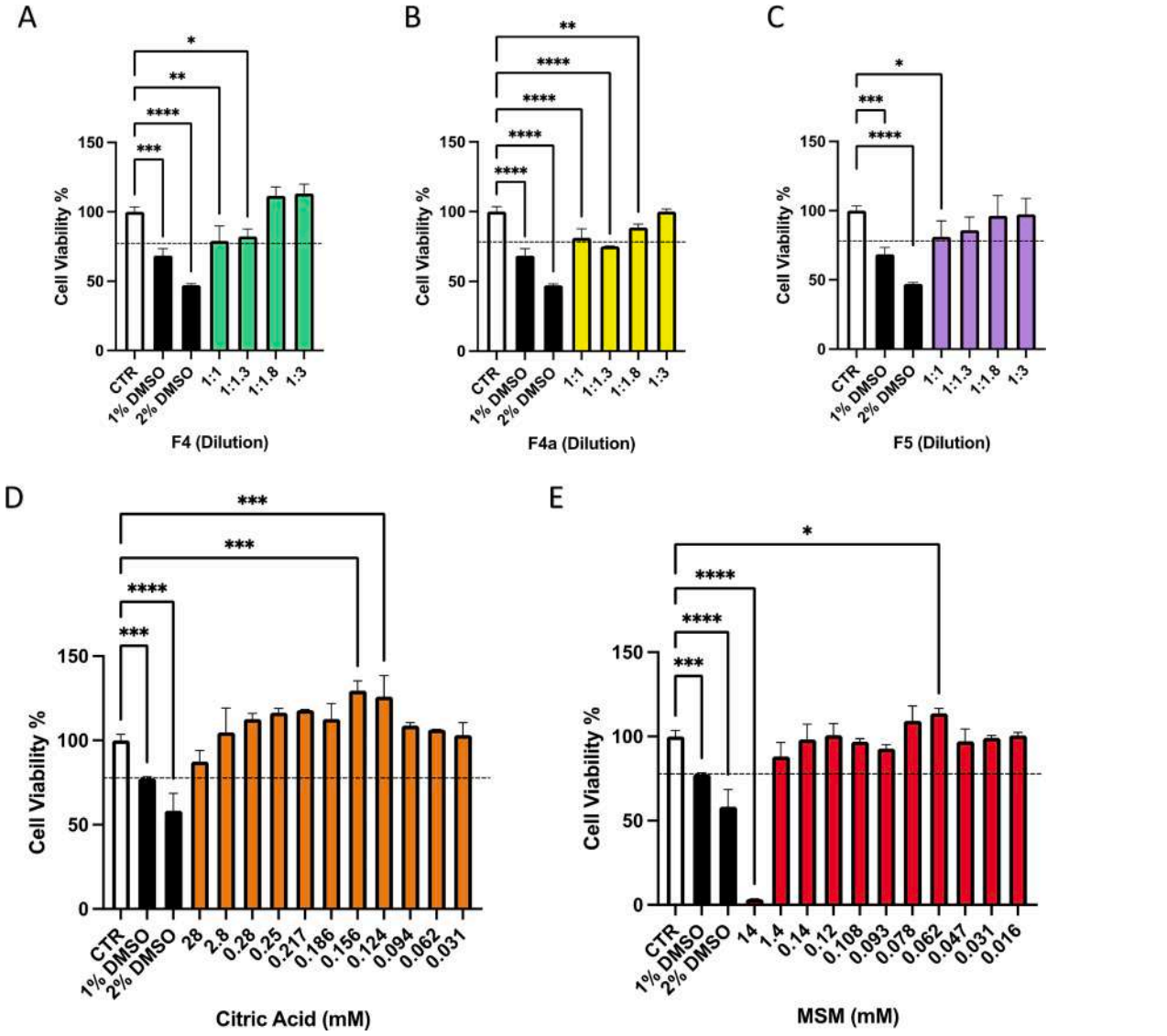

Fig. 2. Viability of HaCaT cells incubated with different dilutions of DMEM at 37 °C overnight with portion of filaments (10 mg in 1 ml) **A**) F4, **B**) F4a, **C**) F5, **D**) Citric Acid, **E**) MSM. The negative control (in white) is represented by untreated cells (CTR) in DMEM and set at 100 %. The positive control (in black) is done with DMSO 1 % and 2 % in DMEM. The percentage of viable cells respect to the control was reported as the mean ± SD of three independent experiments. Dotted lines indicate 80 % cells viability respectively. * $p < 0.01$, ** $p < 0.001$, and *** $p < 0.0001$, treatments versus control (one- way ANOVA test).

composition. The introduction of PCL allowed to improve TPS printability, thus the filaments F4, F4a and F5 were selected for the next studies.

3.2. In vitro effect on cells

The effect on cells viability (safety) was evaluated on keratinocytes, cell line representative of epidermidis. As reported in method section, a portion of each filament was incubated in the culture medium DMEM (10 mg in 1 mL) then, the supernatant was incubated with cells at four different dilutions and the effect on cells viability was evaluated. The obtained results (Fig. 2A-C), show that all the assayed dilutions are safe for cells as the viability measured was $>$ 70 % in all cases.

3.3. Scaffold production

3D printing parameters were optimized in order to produce the scaffold by FDM. In order to achieve a suitable processability of the material, a compromise was found between rigidity of the filament in the nozzle and viscosity of the melt. The process window appears to be rather narrow, however, a previous study [25] showed that it is possible to play with the ageing of the material, since post-crystallisation can be achieved by combination of suitable temperature and relative humidity, thus drying or humidifying the material.

A preliminary bibliographic research was done with the aim to find the most suitable shape for the printing, being that gyroid and honeycomb resulted the most common and useful structures [54,55]. Thus, the first attempt was made with the Infill Pattern "Gyroid" because this structure is effective for wound dressing applications. It was decided to print disk-shaped scaffolds prototypes having a diameter of 20 mm and thickness of 3 mm using an initial infill density of 40 %. However, the gyroid geometry, that requires continuous curvature variations during the printing, does not well suited to the processability of the TPS. Thus, it was decided to use the grid line as infill pattern with more linear geometry useful to facilitate deposition and adhesion of the TPS layers during the printing.

Once selected the shape, scaffold prototypes (Table 3) were produced varying the parameters reported in Table 2 and using F4 composition as a reference. The rationale behind the variations in the parameters was the necessity to find a compromise between material viscosity, stiffness, printing temperature and adequate material flow to allow the melted filament to flow out of the nozzle. In the case of first scaffold (S_01, Table 3), the main problem was the rapid collapse on the plate just after printing and the high plate temperature responsible for browning. To overcome these problems, flow material, print speed and plate temperature were decreased (S_02, Table 3). However, in these conditions, an excessive material flow was observed, thus this parameter was reduced to 60 % (S_03, Table 3), nonetheless no flow was observed in this case. Thus, the parameter was increased to 73 % (S_04, Table 3) and 84 % (S_05, Table 3), even if only the latter variation allowed to print the object (Table 3). In S_05 sample, nozzle temperature and print speed were reduced in parallel to material flow increase. It was observed that TPS filament relaxation occurred even at 190 °C and lower values of print speed allowed a precise printing, achieving the desired infill density (Table 3). The main problem encountered under these working conditions was the difficulty to obtain the interlayer adhesion during the layer to layer deposition. For this reason, the size modification of the scaffold to 15 mm diameter and 1.5 mm thickness (S_06) was considered useful to avoid the use of high material percentages. Since gyroid filling was difficult to be obtained, due to the difficult processability of TPS filament, it was decided to print a lattice structure and, after some attempts in which nozzle T°C, infill density, print speed and fan speed were modified (samples S_7, S_8 and S_9) the most suitable printing conditions were obtained for the scaffold S_10 (Table 3).

The final Infill Line Distance (ILD) was set to 1.7021 mm, by setting an Infill Density (ID) value of 47 % with the Infill Pattern (IP) "grid". This value was obtained from an optimization process of the printing parameters starting from an ID value of 50 %, corresponding to an ILD of 1.6 mm, that allows good mechanical performance (flexibility and resistance) and adequate sizing of the cavities (void coefficient and wall distance) for biological dynamics. Using the setting ID to 50 %, an attempt with the IP "Triangle" was considered, but it was excluded in favor of the grid geometry because setting ID to 50 % in IP "Triangle" resulted in ILDs of 2.4 mm, i.e. wall distances considered less effective for biological dynamics than the grid (Fig. S7, Supplementary Material). However, this sizing creates the external grid walls adhered to the circumferential wall causing solidification and deformation problems during printing with the TPS used (Fig. S8A, Supplementary Material). Thus, it was decided to decrease the ID in order not to stiffen and fill the scaffold, so the first useful value that did not create adhesion/overlap between the external grid lines and the lateral wall was ID 47 % (Fig. S8B, Supplementary Material) and IDL 1.702. Taking into account these considerations, the parameters optimized for scaffold S_10 (Table 3), realized using filament F4, were considered the most suitable and used to produce the 3D printed scaffolds for the next studies (Fig. 3A,B). The same parameters were used to print also the scaffold using the filament F5 (Fig. 3C,D), containing MSM as active ingredient. This confirmed that MSM presence in the filament did not change the material processability. In the case of F4a filament containing low melting PCL, for scaffold printing it was necessary to modify the plate temperature, lowered to 57 °C, due to material collapse (Fig. 3 E,F). The prepared scaffolds, hereinafter called S_10F4 (obtained from F4), S_10F5 (obtained from F5) and S_F4a (obtained from F4a) were then deeply characterized.

3.4. Scaffold characterization

3.4.1. Morphology

The micrographs of the filament's sections show that for both F4 (Fig. 4A) and F5 (Fig. 4C) it is possible to detect the presence of holes, which are not visible in filament F4a (Fig. 4E).

For the scaffolds it is possible to detect the square grids produced by the printing (Fig. 4B, 4D and 4F). The analysis of a surface portion shows that the scaffold produced using filament F4a (S_10F4a) possess a smooth and regular surface (Fig. 4F) while in the case of the other two scaffolds, S_10F4 (Fig. 4B) and S_10F5 (Fig. 4D) a wrinkled and irregular surface is detectable as well as the presence of discontinuities particularly in the case of S_10F5.

3.4.2. Brillouin microscopy

The mechanical properties of the samples were investigated through Brillouin Light Scattering (BLS). Named after Léon Brillouin, who first described the phenomenon in 1922, BLS offers a non-destructive way to probe the elastic properties and dynamic processes in various materials. In BLS, a monochromatic light beam, typically in the visible spectrum, is focused on the sample, where spontaneous time-dependent density fluctuations (acoustic waves or phonons) result in periodic changes in the refractive index, which acts as a diffraction grating for the incoming light and produces a change in its frequency (often in the GHz range), in a way akin to the Doppler effect. BLS detects the position and linewidth of this frequency shift, hence provides direct information about the velocity and nature of the acoustic waves, which in turn are related to the stiffness and internal friction of the material. Typically, the Brillouin spectrum exhibits an intense central peak due to elastically scattered light and a set of equally shifted peaks (the Brillouin doublet) at frequencies $\omega_B = \pm q v_L$.

The latter depend on the longitudinal sound velocity v_L and on the exchanged wavevector $q = (4n\pi/\lambda)\sin(\theta/2)$, where n is the material refractive index, λ the incident wavelength and θ the angle between the incident and scattered light. Therefore, BLS gives direct access to the longitudinal elastic modulus $M = \rho v_L^2$ of the material, provided that n

Table 3
Optimization of 3D printer parameters and visual images of the produced scaffolds.

Sample	Nozzle temperature(° C)	Flow material(%)	Infill density(%)	Print speed(mm/s)	Fan speed(%)	Plate temperature(° C)	ScaffoldImage
S_01	210	88	40	30	30	75	
S_02	220	84	40	25	30	65	
S_03	220	60	40	25	30	65	not printable
S_04	220	73	40	25	30	65	not printable
S_05	215	84	40	20	30	65	
S_06	215	84	40	15	30	65	
S_07	210	84	60	15	30	65	
S_08	208	84	50	10	30	65	
S_09	205	84	45	30	50	65	
S_10	205	84	47	30	50	65	

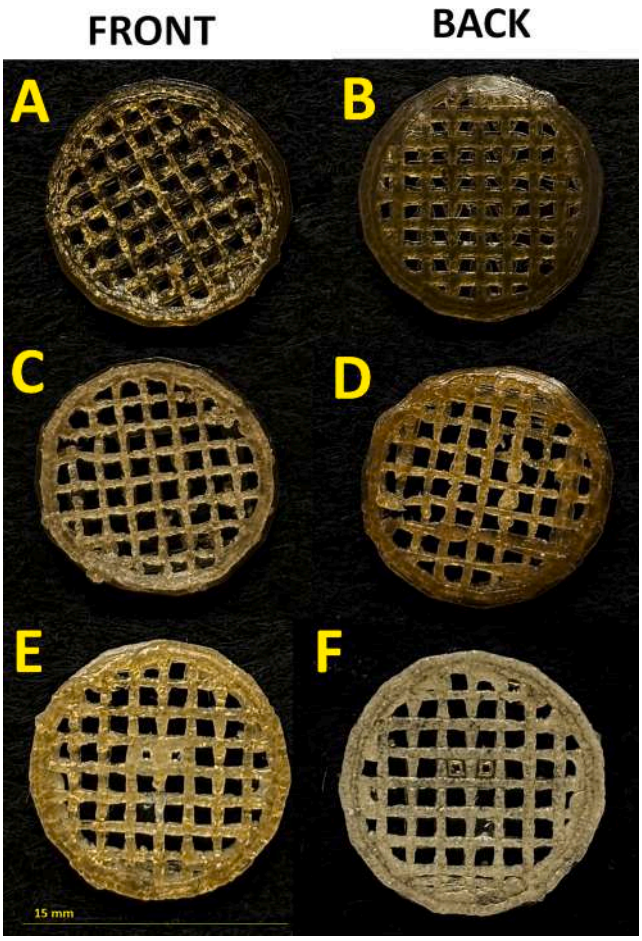

Fig. 3. Pictures of the scaffolds S_10F4 (**A**, **B**), S_10F5 (**C**, **D**) and S_10F4a (**E**, **F**) obtained by using the filaments F4, F5 and F4a, respectively.

and the material density ρ are independently estimated.

In our samples, the refractive index is unknown, but could be estimated from the concentration and density of the various compounds in the filaments. Given the measured value $\rho_{CS} = 0.61$ g/cm^3 for the density of corn starch, and typical values found in the literature for the other compounds, we compute n by using the classical mixing rule described by Lorentz-Lorenz:

$$\frac{n^2-1}{n^2+1} = \sum_i f_i \frac{n_i^2-1}{n_i^2+1} \tag{4}$$

where f_i and n_i are respectively the volume fraction and refractive index of the i-th component of the filament. The results are reported in the Table 4. With these extrapolated values, we compute the exchanged wavevectors in our backscattering configuration $q_{bs} = 4\pi n/\lambda$ and show the results on the rightmost column of the same table.

As evident from the table, the refractive index and thus the exchanged q are almost independent of the resin composition, while the most important variations are observed for the density, the S_10F4a, showing the larger density. Representative Brillouin data acquired in the central part of the samples are shown in Fig. 5A. All the spectra are well captured by a damped harmonic oscillator function (DHO), the typical model used to describe the Brillouin signal from viscoelastic materials:

$$I(\omega) = \frac{I_0}{\pi} \frac{\omega_B^2 \Gamma_B}{\left(\omega^2 - \omega_B^2\right)^2 + \left(\omega\Gamma_B\right)^2} \tag{5}$$

where the fitting parameters are the intensity I_0, the peak position ω_B and width $\Gamma_B = D_k q^2$, where D_k is the kinematic viscosity. The fitting was performed considering the effect of multiple scattering [56], which tends to reduce the definition of the exchanged wavevector q, and the contributions of the q-spread due to the finite numerical aperture of the objective lens. We observed small differences in the data depending on the location on the sample where the spectrum was acquired, probably due to the printing process. As a consequence, we decided to acquire at least five spectra in different points along the sample, from the centre towards the periphery of the printed disks. The results of the Brillouin analysis as a function of sample composition are reported in Fig. 5B. Overall, the data suggest that S_10F4 is the most homogeneous sample, as deduced by the small spread in the Brillouin results, whereas the other samples, S_10F5 and S_10F4a, show broader distributions of values. We report in Fig. 5B(a), and 5B(b) the real M' and imaginary M'' part of the longitudinal modulus. The former is linked to the elasticity of the material as described above, while the latter is related to the linewidth of the peak through $M'' = \omega_B \Gamma_B \rho / q^2$ and gives information on the attenuation of the acoustic waves inside the material.

S_10F4 exhibits the lower elastic modulus among the studied samples ($M' = 8.2 \pm 0.2$ GPa, average $\pm$ standard deviation). On the contrary, addition of PCL increases the stiffness of the printed material, which reaches a value of $M' = 9.3 \pm 0.3$ GPa. The sample S_10F5 displays intermediate rigidity values between S_10F4 and S_10F4a. S_10F4a also displays the highest imaginary part of the longitudinal modulus, while there is an opposite trend between S_10F5 and S_10F4, with S_10F5 showing M'' smaller than S_10F4. These results suggest that the Brillouin response of the printed disks is largely dominated by the density, the refractive index difference only playing a minor role. In order to separate the effect of density and optical properties in the Brillouin analysis, we focus on the Brillouin loss tangent, $\tan(\delta) = M''/M' = \Gamma_B/\omega_B$ [57], which represents the proportion of effective viscosity to stiffness of the microscopic irradiated region and indicates how efficiently energy is stored or dissipated within the material. As evident from the definition, $\tan(\delta)$ does not depend on the sample refractive index and density and thus provides an unbiased estimate of the samples' mechanical properties which does not depend on prior assumptions about density and refractive index. Generally, a high loss tangent signifies greater energy dissipation by the local acoustic waves, suggesting higher viscosity. Conversely, a low loss tangent indicates a higher elasticity in the material and reduced acoustic attenuation. The results of the loss tangent are reported in Fig. 5B(c), confirming the trend of the acoustic speed data (which is independent of ρ), see Fig. 5B(d). From the point of view of internal dynamical process, therefore, the loss tangent analysis suggests increasingly lower phonons attenuation going from sample S_10F4 towards S_10F5, with S_10F4a exhibiting intermediate values.

3.4.3. Swelling and DS%

Scaffolds hydration capacity and erosion were evaluated according to Eq. (2) and Eq. (3) respectively for a period of 20 days, average time in which a deep wound starts to heal [58].

Considering the positioning of the scaffold in a deep wound (e.g. diabetic foot ulcers), the study of scaffold swelling capacity gives information about the stability (integrity of the structure) when in contact with biological fluids, necessary to allow cells colonization and thus tissue regeneration. The obtained results (Fig. 6A) show that S_10F4 swells gradually, reaching ~ 18 % of hydration after 1 day and ~ 35 % after 7 days. The slow hydration could be attributed to starch structure after plasticization, consisting both of thermoplastic soluble (amylose) and insoluble (amylopectin) fractions. The latter, exposed in the external part of plasticized starch granules, is responsible for the slow fluid penetration and thus for the limited swelling observed. After 7 days the swelling value decreases due to the erosion phenomena (Fig. 6B), mainly attributable to starch fragmentation as well as to CA solubilization. In the case of S_10F4a a rapid swelling is observable due to PCL presence in the composition, reaching 45 % of hydration in the first day. The value then decreases reaching ~ 35 % at 20th day, attributable to

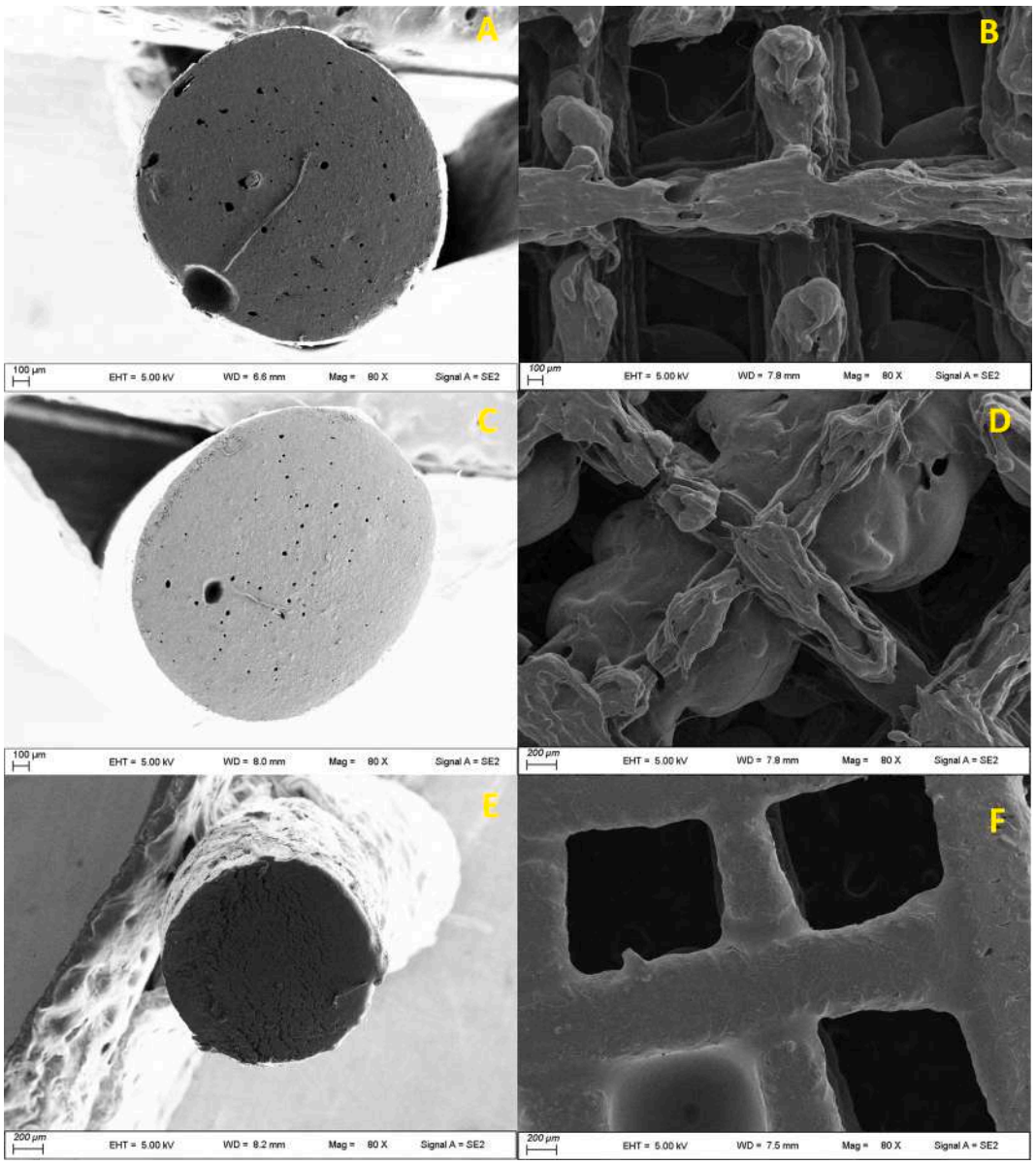

Fig. 4. SEM micrographs of: **A**) section of filament F4; **B**) grid open S_10F4; **C**), section of filament F5; **D**) grid open S_10F5; **E**) section of filament F4a and **F**) grid open S_10F4a. Magnification 80X.

Table 4
Refractive index and q_{bs} obtained for the prepared scaffolds.

Sample	Density (g/cm^3)	Refractive Index *n*	q_{bs} (nm^{-1})
S_10F4	0.745	1.4963	0.03534
S_10F5	0.820	1.4935	0.03531
S_10F4a	0.751	1.4950	0.03527

the gradual erosion to which the scaffold undergoes, mainly attributable to both starch fragmentation and CA solubilization. The profile is similar to that obtained for S_10F4, suggesting that the influence of PCL in the erosion process in negligible (Fig. 6B).

For the scaffold S_10F5 the measurements were not possible because it underwent to disaggregation with consequent loss of the integrity as shown in the picture reported in Fig. 6D. This could be ascribed to the different characteristics the scaffold. By the SEM micrographs registered for S_10F5 (Fig. 4D) it is possible to observe the presence of discontinuities and irregularities responsible for a rapid water penetration in the inner spaces and consequent breaking. However, it should be considered that the scaffold, once placed in the wound bed, may not be really immersed in a large volume of fluid (as the condition in which the experiment was performed). Thus, for S_10F5 should be considered optimal the use in poor exuding wounds in which its integrity could be maintained. For S_10F4 and S_10F4a the scaffold is still visible and intact after incubation in SWF (Fig. 6C and 6E, respectively).

3.4.4. *Wound healing assay*

An *in vitro* wound healing experiment was planned and executed to assess scaffold capability to favour the healing process. Each scaffold was incubated with DMEM, as described in method section, and the supernatant, both undiluted and diluted, was incubated with cells. The most interesting results were obtained for all the scaffolds using the dilution 1:1.8. In all cases in fact (Fig. 7A) an almost complete closure of the wound was observed after 24 hrs in comparison to the control (cells incubated with just DMEM). In order to better understand the main factor responsible for the observed effect, a preliminary evaluation was performed considering the components used for the filaments used for scaffolds production. In all cases, namely F4, F4a and F5 compositions,

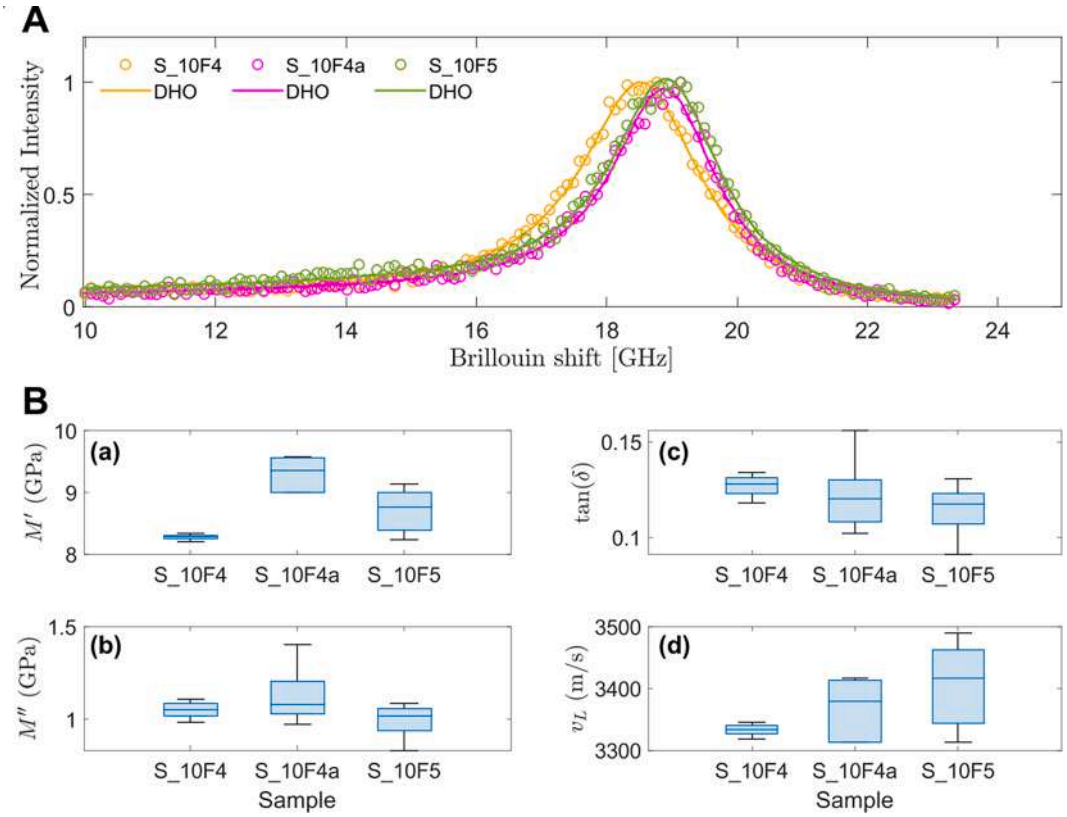

Fig. 5. **A**) Typical Brillouin spectra of our samples and the DHO fits; **B**) The real (**a**) and imaginary (**b**) part of the longitudinal modulus. (**c**) The loss tangent $\tan(\delta) = M''/M'$ and (**d**) acoustic longitudinal speed v_L. For each chart, the line inside the box represents the median of five measurements at different sample locations, the top and bottom edges are the upper and lower quartiles, while the whiskers connect the upper and lower quartiles to respectively the maximum and minimum values that are not outliers.

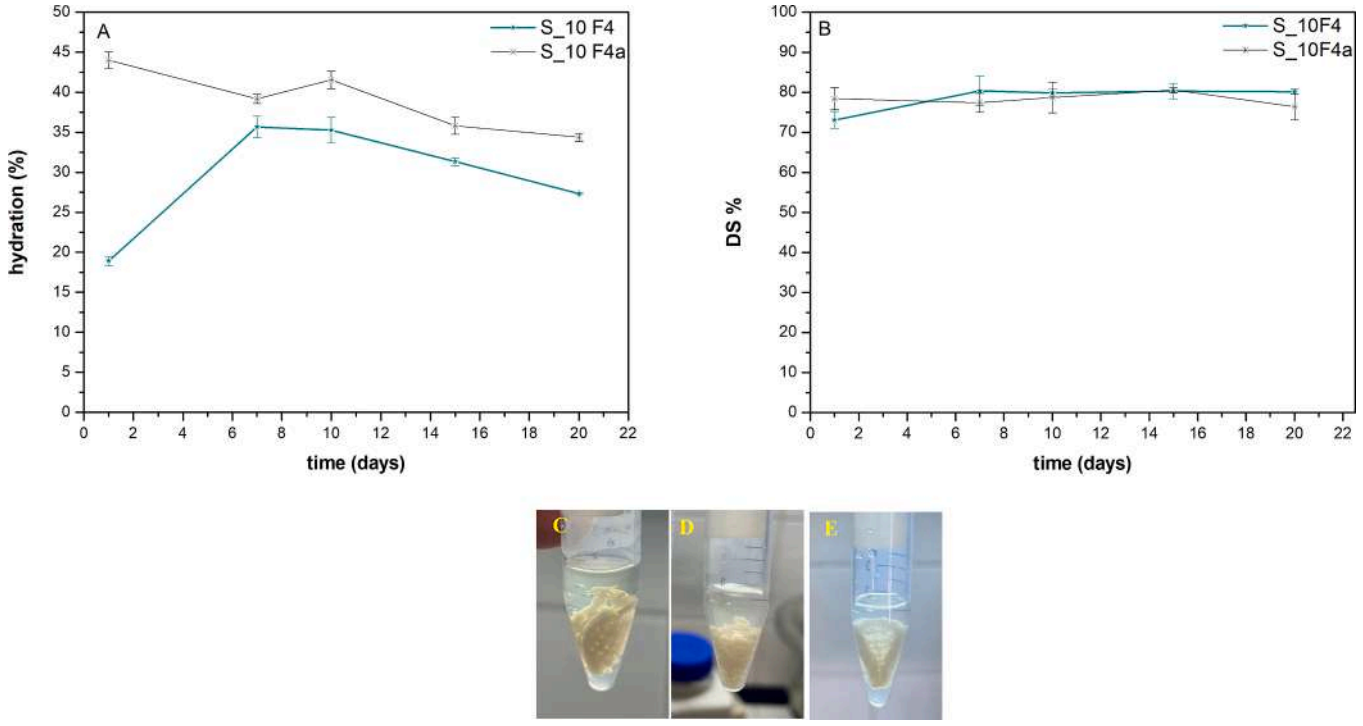

Fig. 6. Results of **A**) hydration (%) and **B**) Swelling Degree (DS, %) obtained for S_10F4 and S_F4a. Pictures of the prepared scaffolds after contact with SWF for 24 h: (**C**) S_10F4, (**D**) S_10F5, (**E**) S_F4a.

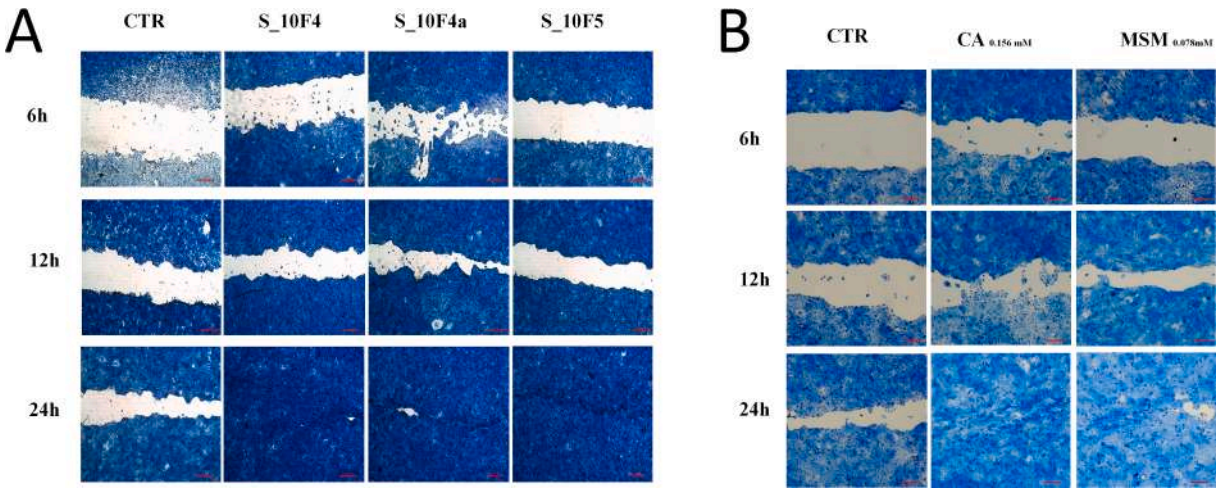

Fig. 7. Results of scratch assay performed on the dilutions 1:1.8 of the solutions obtained from the three different scaffolds incubated with DMEM at 37 °C overnight. Wound field observed at 6, 12 and 24 h. The scale bar (in red) represents 200 μm.

starch, Gly and CA were used, MSM was also present in F5 (Table 1). As in literature it is reported that CA possess ability to stimulate cell growth by creating an acidic environment [59], this aspect was taken into consideration and evaluated. Thus, a subsequent experiment was performed on CA alone reproducing the same concentration obtained from the incubation of the scaffolds with DMEM and quantified by NMR (Table S2).

In first instance, MTT assay was carried out in order to assess the safety on HaCat cells using a concentration range of CA between 0.031 mM and 28 mM in complete DMEM (Fig. 2D). All concentrations tested resulted completely safe *in vitro*. Then, the wound healing assay was performed as well and the complete wound field closure was obtained using the concentration 0.156 mM (corresponding to the dilution 1:1.8 resulted effective for the scaffold) (Fig. 7B). This result confirmed CA contribution to the observed wound healing capacity of the scaffolds. As S_10F5 differs from the other two scaffolds for the MSM presence, the evaluation of MSM effect alone on keratinocytes was considered useful to assess.

From MTT assay (Fig. 2E) emerged that concentrations from 0.016 to 1.4 mM are safe for cells. The wound healing assays were performed starting from the concentration 0.14 mM to 0.068 mM produced from scaffold incubation with DMEM for 24 h and measured by NMR. Also in this case, the best result was obtain using 0.078 mM of MSM which corresponds to the dilution responsible for the wound field closure observed for the scaffold (Fig. 7B). The obtained results are very interesting, suggesting that the use of F4 is suitable to obtain a scaffold (S_F4) capable of stimulating the healing process. The scaffold prepared with F5 (S_F5), due to MSM presence, should stimulate the wound healing and at the same time could control the inflammation processes due to the well-known anti-inflammatory effect of this molecule [60].

3.4.5. Antimicrobial activity

Wounds can very often be colonised by bacteria which are responsible for local infections that hinder wound healing and may also cause subsequent systemic infections. Therefore, antimicrobial treatment is required. For this reason, the scaffold's antimicrobial activity was also evaluated. A preliminary study performed on the starting filaments (Table S3, Supplementary Material), showed that all the filaments are active against *S. pyogenes*, a pathogenic responsible for a high percentages of skin and soft tissue infections [61], whose treatment by conventional antibiotics is often unsuccessful due to antimicrobial resistance problems [62].

The same experiment was performed on the prepared scaffolds in order to evaluate their effect on *S. pyogenes*. The obtained results (Fig. 8) show the following inhibition halos: 20.01 mm (S_10F5), 22.02 mm (S_10F4a) and 24.74 mm (S_10F4), suggesting a possible application for the treatment of deep infected wounds.

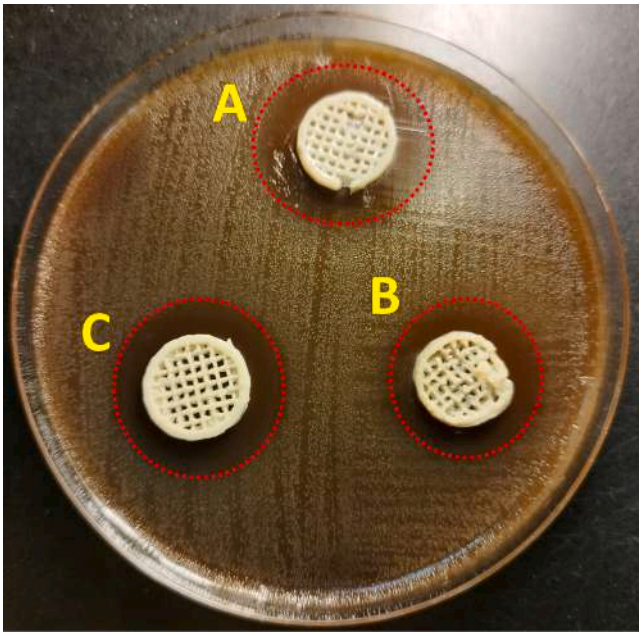

Fig. 8. Inhibition halos (mm) obtained incubating S_10F4 (**A**), S_10F5 (**B**), and S_10F4a (**C**) with *S. pyogenes*.

Also in this case the explanation of the observed effect can be found in one of the common components of the three scaffolds, in particular it can be attributable to CA, which antimicrobial activity has been well proven [63]. Thanks to its acidification effect on the culture medium, in fact, it is able to cause the disruption of the bacteria cell membrane with consequent bactericidal effect.

4. Conclusions

This work demonstrated the feasibility of fabricating thermoplastic starch filaments (TPS) suitable for Fusion Deposition Modelling 3D printing technique. The combination of high corn-starch amounts (70 % w/w) to glycerol and other additives as montmorillonite, magnesium stearate and citric acid allowed to obtain processable filaments

overcoming TPS limitations. The presence of polycaprolactone or the inorganic thermostable molecule methyl sulfonyl methane, used as model drug, was evaluated as well. Scaffolds with grid line geometry were fabricated. All demonstrated ability to absorb artificial exudate. The composition containing PCL, as expected, demonstrated better integrity. In vitro studies performed on keratinocytes confirmed that the developed formulations are safe for cells and able to stimulate keratinocytes growth useful to enhance the wound healing process. Additionally, the proved antimicrobial activity observed against *S. pyogenes*, one of the most common bacteria involved in wound infection, suggests that the projected formulation could be a useful tool in the scenario of formulations for wound treatment. In a broader perspective, the filaments could be customized introducing thermostable active pharmaceutical ingredients for the production of scaffold for other applications.

The purposed formulation can also be considered sustainable as produced using eco-friendly ingredients. Moreover, the production of the final formulation and its disposal, after use, does not produce any pollution and wastes. The strength is represented by the fact that the research of human health takes place in the total respect of the animals and environment, fully inserted into the concept of one-health.

CRediT authorship contribution statement

Franco Dominici: Methodology, Investigation, Data curation, Conceptualization. **Anna Imbriano:** Writing – original draft, Methodology, Investigation, Data curation. **Debora Puglia:** Writing – review & editing, Supervision, Resources, Project administration, Funding acquisition, Conceptualization. **Cinzia Pagano:** Writing – review & editing, Writing – original draft, Visualization, Validation, Supervision, Project administration, Methodology, Investigation, Funding acquisition, Data curation, Conceptualization. **Francesca Luzi:** Formal analysis, Data curation. **Aurora Rafanelli:** Investigation, Data curation. **Alessandro Di Michele:** Formal analysis, Data curation. **Francesco Bonacci:** Investigation, Formal analysis, Data curation. **Maria Rachele Ceccarini:** Investigation, Formal analysis, Data curation. **Sara Primavilla:** Investigation, Formal analysis, Data curation. **Andrea Valiani:** Resources, Funding acquisition. **Leonardo Tensi:** Formal analysis, Data curation. **Carmen Laura Pérez Gutierrez:** Investigation, Formal analysis, Data curation. **Raquel De Melo Barbosa:** Writing – original draft, Visualization. **César Viseras:** Visualization, Validation, Supervision, Resources, Project administration, Methodology. **Maurizio Ricci:** Visualization, Resources, Funding acquisition. **Luana Perioli:** Writing – review & editing, Writing – original draft, Visualization, Validation, Supervision, Resources, Project administration, Funding acquisition, Methodology, Conceptualization.

Declaration of competing interest

The authors declare that they have no known competing financial interests or personal relationships that could have appeared to influence the work reported in this paper.

Acknowledgements

This work was funded by: the European Union—NextGenerationEU under the Italian Ministry of University and Research (MUR) National Innovation Ecosystem grant ECS00000041—VITALITY. We acknowledge the Università degli Studi di Perugia, Università Politecnica delle Marche and MUR for support within the project Vitality;

The Spanish Project PID2022-137603013–100 (Ministerio de Ciencia, Innovación y Universidades). Recipient: Prof. César Viseras;

The EMERGIA Program Project 2022/00001046 (Junta de Andalucía), Recipient: Prof. Raquel de Melo Barbosa.

Authors sincerely acknowledge Mr. Marco Marani from the Department of Pharmaceutical Sciences of the University of Perugia for technical assistance.

Appendix A. Supplementary data

Supplementary data to this article can be found online at https://doi.org/10.1016/j.ejpb.2025.114698.

Data availability

Data will be made available on request.

References

[1] S. Cailleaux, N.M. Sanchez-Ballester, Y.A. Gueche, B. Bataille, I. Soulairol, Fused Deposition Modeling (FDM), the new asset for the production of tailored medicines, J. Control. Release 330 (2021) 821–841.
[2] I. Buj-Corral, A. Tejo-Otero, F. Fenollosa-Artés, Use of FDM Technology in Healthcare Applications: Recent Advances, in: H.K. Dave, J.P. Davim (Eds.), Fused Deposition Modeling Based 3D Printing, Springer, Cham, 2021, pp. 277–297.
[3] K. Glover, E. Mathew, G. Pitzanti, E. Magee, D.A. Lamprou, 3D bioprinted scaffolds for diabetic wound-healing applications, Drug Deliv, Transl. Res. 13 (2023) 2096–2109.
[4] Y. Sun, A.D. Juncos Bombin, P. Boyd, N. Dunne, H.O. McCarthy, Application of 3D printing & 3D bioprinting for promoting cutaneous wound regeneration, Bioprinting. 28 (2022) e00230.
[5] P.E. Antezana, S. Municoy, M.I. Álvarez-Echazú, P.L. Santo-Orihuela, P. N. Catalano, T.H. Al-Tel, F.B. Kadumudi, A. Dolatshahi-Pirouz, G. Orive, M. F. Desimone, The 3D Bioprinted Scaffolds for Wound Healing, Pharmaceutics. 14 (2022) 464.
[6] D.T. Uchida, M.L. Bruschi, 3D Printing as a Technological Strategy for the Personalized Treatment of Wound Healing, AAPS PharmSciTech 24 (2023) 41.
[7] R.B. Kristiawan, F. Imaduddin, D. Ariawan, Z.A. Ubaidillah, A review on the fused deposition modeling (FDM) 3D printing: Filament processing, materials, and printing parameters, Open Eng. 11 (2021) 639–649.
[8] A.M.E. Arefin, N.R. Khatri, N. Kulkarni, P.F. Egan, Polymer 3D printing review: Materials, process, and design strategies for medical applications, Polymers (Basel). 13 (2021) 1499.
[9] T. Pepelnjak, J. Stojšić, L. Sevšek, D. Movrin, M. Milutinović, Influence of Process Parameters on the Characteristics of Additively Manufactured Parts Made from Advanced Biopolymers, Polymers (Basel). 15 (2023) 716.
[10] A. Sadeghianmaryan, N. Ahmadian, S. Wheatley, H.A. Sardroud, S.A. Seyyed Nasrollah, E. Naseri, A. Ahmadi, Advancements in 3D-printable polysaccharides, proteins, and synthetic polymers for wound dressing and skin scaffolding – A review, Int. J. Biol. Macromol. 266 (2024) 131207.
[11] B.D. Patil, K.P. Chamate, N.V. Bhosale, N.V. Desai, P.V. Kadam, A. Sanap, A. Kharat, S. Kheur, R.V. Badh, A Comprehensive Exploration of Polymeric 3D Sponges for Regeneration of Bone, Regen. Eng. Transl. Med. (2025).
[12] S. Vach Agocsova, M. Culenova, I. Birova, L. Omanikova, B. Moncmanova, L. Danisovic, S. Ziaran, D. Bakos, P. Alexy, Resorbable Biomaterials Used for 3D Scaffolds in Tissue Engineering: A Review, Materials (Basel) 16 (2023) 4267.
[13] Z. Qiu, B. Zheng, J. Xu, J. Chen, L. Chen, 3D-printing of oxidized starch-based hydrogels with superior hydration properties, Carbohydr. Polym. 292 (2022) 119686.
[14] Y. Zhang, J. Lv, Z. Qiu, L. Chen, Influence of carboxyl content on the rheological properties and printability of oxidized starch for 3D printing applications, Int. J. Biol. Macromol. 289 (2025) 138794.
[15] F. Hernandez-Tenorio, E. Múnera-Gutiérrez, A.M. Miranda, A.A. Sáez, L.D. Marín-Palacio, C. Giraldo-Estrada, 3D printing of polysaccharide-based formulations: Opportunities for innovation, Bioprinting. 45 (2025) e00383.
[16] A. Joseph, A.S. Vijayan, J. Xavier, M. KB, A. Karthikeyan, N. Gopinath, M. PV, B. G. Nair, 3D printed arrowroot starch-gellan scaffolds for wound healing applications, Int. J. Biol. Macromol. 264 (2024) 130604.
[17] K. González, I. Larraza, G. Berra, A. Eceiza, N. Gabilondo, 3D printing of customized all-starch tablets with combined release kinetics, Int. J. Pharm. 622 (2022) 121872.
[18] L. Rong, X. Chen, M. Shen, J. Yang, X. Qi, Y. Li, J. Xie, The application of 3D printing technology on starch-based product: A review, Trends Food Sci. Technol. 134 (2023) 149–161.
[19] H. Mahani, M. Karevan, M. Safavi, On the Biodegradable Polylactic Acid (Pla)/ Thermoplastic Starch (Tps)/Nanoclay Based Nanocomposites Used in Fused-Filament 3d Printing, SSRN Electron. J. (2022).
[20] Q. Ju, Z. Tang, H. Shi, Y. Zhu, Y. Shen, T. Wang, Thermoplastic starch based blends as a highly renewable filament for fused deposition modeling 3D printing, Int. J. Biol. Macromol. 219 (2022) 175–184.
[21] Z. Ni, J. Shi, M. Li, W. Lei, W. Yu, FDM 3D Printing and Soil-Burial-Degradation Behaviors of Residue of Astragalus Particles/Thermoplastic Starch/Poly(lactic acid) Biocomposites, Polymers (Basel). 15 (2023) 2382.
[22] Y.Q. Zhao, J.H. Yang, X. Ding, X. Ding, S. Duan, F.J. Xu, Polycaprolactone/ polysaccharide functional composites for low-temperature fused deposition modelling, Bioact. Mater. 5 (2020) 185–191.
[23] M. Trebuňová, P. Petroušková, A.F. Balogová, G. Ižaríková, P. Horňak, D. Bačenková, J. Demeterová, J. Živčák, Evaluation of Biocompatibility of PLA/ PHB/TPS Polymer Scaffolds with Different Additives of ATBC and OLA Plasticizers, J. Funct. Biomater. 14 (2023) 412.

[24] C.L. Pérez Gutiérrez, F. Dominici, F. Luzi, D. Puglia, F. Cottone, A. Di Michele, C. Pagano, C.A. Viseras Iborra, L. Perioli, Development of filaments based on thermoplastic starch and cationic clays suitable for Fused Deposition Modelling, in: 11th International Colloids Conference, Hannah Griffiths for and on behalf of Elsevier Ltd., 2022.
[25] C.L.P. Gutiérrez, F. Dominici, F. Luzi, D. Puglia, A. Di Michele, F. Cottone, C. Pagano, C. Viséras, L. Perioli, Thermoplastic corn starch reinforced with different additives for 3D printed application, in: Interregional Meeting of the Italian Chemical Society-Section Toscana, Umbria, Marche and Abruzzo (TUMA 2022), Società Chimica Italiana, 2022.
[26] R.J. Young, P.A. Lovell (Eds.), Introduction to Polymers, Third Edition, CRC Press, Boca Raton, 2011.
[27] Z.Q. Fu, L.J. Wang, D. Li, Y.G. Zhou, B. Adhikari, The effect of partial gelatinization of corn starch on its retrogradation, Carbohydr. Polym. 97 (2013) 512–517.
[28] S. Mattana, M. Mattarelli, L. Urbanelli, K. Sagini, C. Emiliani, M.D. Serra, D. Fioretto, S. Caponi, Non-contact mechanical and chemical analysis of single living cells by microspectroscopic techniques, Light Sci. Appl. 7 (2018) page17139.
[29] A. Di Michele, C.L.P. Gutiérrez, C. Pagano, T. Beccari, M.R. Ceccarini, F. Luzi, D. Puglia, L. Tensi, E. D'Agosto, C.A.V. Iborra, M. Ricci, L. Perioli, Formulation and characterization of sustainable bioadhesive films for wound treatment based on barley β-glucan extract obtained using the high power ultrasonic technique, Int. J. Pharm. 638 (2023) 122925.
[30] S. Primavilla, C. Pagano, R. Roila, R. Branciari, D. Ranucci, A. Valiani, M. Ricci, L. Perioli, Antibacterial Activity of Crocus sativus L. Petals Extracts against Foodborne Pathogenic and Spoilage Microorganisms, with a Special Focus on Clostridia, Life. 13 (2023) 60.
[31] A. Amirkiai, M. Panahi-Sarmad, G.M.M. Sadeghi, M. Arjmand, M. Abrisham, P. Dehghan, H. Nazockdast, Microstructural design for enhanced mechanical and shape memory performance of polyurethane nanocomposites: Role of hybrid nanofillers of montmorillonite and halloysite nanotube, Appl. Clay Sci. 198 (2020) 105816.
[32] T.S. Gaaz, A.B. Sulong, A.A.H. Kadhum, A.A. Al-Amiery, M.H. Nassir, A.H. Jaaz, The impact of halloysite on the thermo-mechanical properties of polymer composites, Molecules 22 (2017) 838.
[33] J. Pumchusak, N. Thajina, W. Keawsujai, P. Chaiwan, Effect of organo-modified montmorillonite nanoclay on mechanical, thermo-mechanical, and thermal properties of carbon fiber-reinforced phenolic composites, Polymers (Basel). 13 (2021) 754.
[34] Y. Jiugao, W. Ning, M. Xiaofei, The effects of citric acid on the properties of thermoplastic starch plasticized by glycerol, Starch/Staerke 57 (2005) 494–504.
[35] M. Butawan, R.L. Benjamin, R.J. Bloomer, Methylsulfonylmethane: Applications and safety of a novel dietary supplement, Nutrients 9 (2017) 290.
[36] J. Ren, K.M. Dang, E. Pollet, L. Avérous, Preparation and characterization of thermoplastic potato starch/halloysite nano-biocomposites: Effect of plasticizer nature and nanoclay content, Polymers (Basel). 10 (2018) 808.
[37] A. Ghanbari, T. Tabarsa, A. Ashori, A. Shakeri, M. Mashkour, Preparation and characterization of thermoplastic starch and cellulose nanofibers as green nanocomposites: Extrusion processing, Int. J. Biol. Macromol. 112 (2018) 442–447.
[38] S.C. Lara, F. Salcedo, Gelatinization and retrogradation phenomena in starch/montmorillonite nanocomposites plasticized with different glycerol/water ratios, Carbohydr. Polym. 151 (2016) 206–212.
[39] M. Combrzyński, T. Oniszczuk, K. Kupryaniuk, A. Wójtowicz, M. Mitrus, M. Milanowski, J. Soja, I. Budziak-Wieczorek, D. Karcz, D. Kamiński, S. Kulesza, K. Wojtunik-Kulesza, K. Kasprzak-Drozd, M. Gancarz, I. Kowalska, L. Ślusarczyk, A. Matwijczuk, Physical properties, spectroscopic, microscopic, x-ray, and chemometric analysis of starch films enriched with selected functional additives, Materials (Basel). 14 (2021) 2673.
[40] X. Ma, P.R. Chang, J. Yu, M. Stumborg, Properties of biodegradable citric acid-modified granular starch/thermoplastic pea starch composites, Carbohydr. Polym. 75 (2009) 1–8.
[41] A. Willfahrt, E. Steiner, J. Hötzel, X. Crispin, Printable acid-modified corn starch as non-toxic, disposable hydrogel-polymer electrolyte in supercapacitors, Appl. Phys. A Mater. Sci. Process. 125 (2019) 474.
[42] R.C. Rowe, P.J. Sheskey, M.E. Fenton (Eds.), Handbook of Pharmaceutical Excipients, seventh edition, Pharmaceutical Press, London, 2012.
[43] J.H. Mina Hernandez, Effect of the incorporation of polycaprolactone (Pcl) on the retrogradation of binary blends with cassava thermoplastic starch (tps), Polymers (Basel) 13 (2021) 38.
[44] N. Mutis González, P. Pineda Gómez, M.E. Rodríguez García, Effect of the addition of potassium and magnesium ions on the thermal, pasting, and functional properties of plantain starch (Musa paradisiaca), Int. J. Biol. Macromol. 124 (2019) 41–49.
[45] E. Carazo, A. Borrego-Sánchez, F. García-Villén, R. Sánchez-Espejo, C. Aguzzi, C. Viseras, C.I. Sainz-Díaz, P. Cerezo, Assessment of halloysite nanotubes as vehicles of isoniazid, Colloids Surfaces B Biointerfaces. 160 (2017) 337–344.
[46] F. García-Villén, A. Faccendini, C. Aguzzi, P. Cerezo, M.C. Bonferoni, S. Rossi, P. Grisoli, M. Ruggeri, F. Ferrari, G. Sandri, C. Viseras, Montmorillonite-norfloxacin nanocomposite intended for healing of infected wounds, Int. J. Nanomedicine. 14 (2019) 5051–5060.
[47] M. Zhang, H. Chen, Development and characterization of starch-sodium alginate-montmorillonite biodegradable antibacterial films, Int. J. Biol. Macromol. 233 (2023) 123462.
[48] P. González Seligra, C. Medina Jaramillo, L. Famá, S. Goyanes, Data of thermal degradation and dynamic mechanical properties of starch-glycerol based films with citric acid as crosslinking agent, Data Br. 7 (2016) 1331–1334.
[49] R. Swain, S. Nandi, S. Mohapatra, S. Mallick, Engineered Clay-Polymer Composite for Biomedical Drug Delivery and Future Challenges: A Survey, Curr. Drug Deliv. 21 (2023) 645–661.
[50] Z.U. Arif, M.Y. Khalid, R. Noroozi, M. Hossain, H.T.H. Shi, A. Tariq, S. Ramakrishna, R. Umer, Additive manufacturing of sustainable biomaterials for biomedical applications, Asian J. Pharm. Sci. 18 (2023) 100812.
[51] N. Raina, R. Pahwa, J.K. Khosla, P.N. Gupta, M. Gupta, Polycaprolactone-based materials in wound healing applications, Polym. Bull. 79 (2022) 7041–7063.
[52] T.K. Dash, V.B. Konkimalla, Polymeric modification and its implication in drug delivery: Poly-ε-caprolactone (PCL) as a model polymer, Mol. Pharm. 9 (2012) 2365–2379.
[53] S. Holešová, K. Čech Barabaszová, M. Hundáková, G. Kratošová, V. Kaloč, K. Joszko, B. Gzik-Zroska, Comprehensive study of antimicrobial polycaprolactone/clay nanocomposite films: Preparation, characterization, properties and degradation in simulated body fluid, Polym. Compos. 45 (2024) 9280–9298.
[54] G. Dubinenko, A. Zinoviev, E. Bolbasov, A. Kozelskaya, E. Shesterikov, V. Novikov, S. Tverdokhlebov, Highly filled poly(l-lactic acid)/hydroxyapatite composite for 3D printing of personalized bone tissue engineering scaffolds, J. Appl. Polym. Sci. 138 (2021) 49662.
[55] G. Ehrmann, A. Ehrmann, Shape-memory properties of 3D printed PLA structures, in: Proceedings, Vol. 69, No. 1, MDPI, 2020, p. 6.
[56] M. Mattarelli, G. Capponi, A.A. Passeri, D. Fioretto, S. Caponi, Disentanglement of Multiple Scattering Contribution in Brillouin Microscopy, ACS Photonics 9 (2022) 2087–2091.
[57] G. Perna, F. Bonacci, S. Caponi, G. Clementi, A. Di Michele, L. Gammaitoni, M. Mattarelli, I. Neri, D. Puglia, F. Cottone, 3D-Printed Piezoelectret Based on Foamed Polylactic Acid for Energy-Harvesting and Sensing Applications, Nanomaterials 13 (2023) 2953.
[58] E.M. Tottoli, R. Dorati, I. Genta, E. Chiesa, S. Pisani, B. Conti, Skin wound healing process and new emerging technologies for skin wound care and regeneration, Pharmaceutics. 12 (2020) 735.
[59] P. Sim, X.L. Strudwick, Y.M. Song, A.J. Cowin, S. Garg, Influence of Acidic pH on Wound Healing In Vivo: A Novel Perspective for Wound Treatment, Int. J. Mol. Sci. 23 (2022) 13655.
[60] H.L. Jeong, E. Bin Kang, S.G. Yun, D.B. Park, J.O. Lim, J.S. Suh, Effect of a Silk Sericin and Methylsulfonylmethane (MSM) Blends on Inflammatory Response and Wound Healing, Appl. Sci. 13 (2023) 288.
[61] D.L. Stevens, A.E. Bryant, Streptococcus pyogenes Impetigo, Erysipelas, and Cellulitis, in: D.L. Stevens, A.E. Bryant, J.J. Ferretti, D.L. Stevens, V.A. Fischetti (Eds.), Streptococcus pyogenes: Basic Biology to Clinical Manifestations, 2nd edition, Oklahoma City, Chapter 23, 2022.
[62] V. Cattoir, Mechanisms of Streptococcus pyogenes Antibiotic Resistance, in: Streptococcus pyogenes: Basic Biology to Clinical Manifestations, 2nd edition, Oklahoma City, University of Oklahoma Health Sciences Center, Chapter 30, 2022.
[63] H.B. Coban, Organic acids as antimicrobial food agents: applications and microbial productions, Bioprocess Biosyst. Eng. 43 (2020) 569–591.